# Studies of electron transfer in NaI with pump–probe femtosecond photoelectron spectroscopy

Yasuki Arasaki and Kazuo Takatsuka[a)]
*Department of Basic Science, Graduate School of Arts and Sciences, University of Tokyo, Komaba, 153-8902, Tokyo, Japan*

Kwanghsi Wang and Vincent McKoy[b)]
*Laboratory for Molecular Sciences, California Institute of Technology, Pasadena, California 91125*

(Received 5 June 2003; accepted 24 July 2003)

We discuss an extension of our formulation of energy- and angle-resolved photoelectron spectra for femtosecond pump–probe ionization of wave packets to nonadiabatically coupled states and present results of its applications to wave packet motion on the ionic ($Na^+I^-$) and covalent (NaI) states of sodium iodide. The results of these studies suggest that the energy and angular distributions of these photoelectron spectra provide a useful mapping of the bifurcation of the wave packets through the crossing region and a valuable window on the intramolecular electron transfer occurring between the covalent and ionic states ($NaI \rightarrow Na^+I^-$). © *2003 American Institute of Physics.*
[DOI: 10.1063/1.1609397]

## I. INTRODUCTION

Numerous studies have shown pump-probe femtosecond photoelectron spectroscopy to be a useful probe of wave packet dynamics in molecular systems.[1–12] In this technique, a femtosecond pulse (pump) is used to prepare a wave packet on an excited state which is subsequently probed by ionization with another pulse (probe). These pump–probe energy-resolved photoelectron spectra are well suited for monitoring wave packet motion and evolution of the associated electronic structure along all energetically allowed internuclear distances simultaneously.[1,2,4–8] Furthermore, the angular distributions of the photoelectrons can convey rich insight into the underlying wave packet dynamics.[8,9,13–16]

Efforts to map vibrational wave packets with the aid of femtosecond pump–probe energy-resolved photoelectron spectra were stimulated by the seminal studies of Engel and co-workers[2,17] who showed how the dynamics of a vibrational wave packet, including reflection and splitting at a potential barrier, could be seen in the time-dependent photoelectron energy distributions. This was illustrated for the case of wave packet motion on the $^1\Sigma_u^+$ double-minimum potential in $Na_2$ that arises from the avoided crossing of diabatic states.[17] In recent papers we developed a theory of energy- and angle-resolved photoelectron spectra for femtosecond pump–probe ionization of wave packets in molecules and employed this formulation in studies of wave packets on this double-minimum state of $Na_2$.[13,15,18,19] In contrast to previous studies,[2,17] these studies used geometry- and energy-dependent photoionization amplitudes obtained with high-quality wave functions for the double-minimum state and for the photoelectron continuum. The results highlighted the importance of a robust description of the photoionization dynamics and its dependence on geometry in studies of pump–probe photoelectron spectra of wave packets in regions of avoided crossing where the electronic wave function evolves rapidly with geometry.

In this paper we extend our work to study wave packet motion on the nonadiabatically coupled ionic ($Na^+I^-$) and covalent (NaI) states of sodium iodide. A principal objective of these studies is to explore the potential utility of energy- and angle-resolved pump–probe photoelectron spectroscopy for direct observation of wave packet bifurcation due to a nonadiabatic transition and for monitoring the electron transfer that occurs as the wave packet passes through the avoided crossing between the ionic and covalent potentials of NaI. The present studies differ from our earlier work which simply mapped vibrational wave packets on a single potential curve.

A brief outline of the paper is as follows. We first develop the requisite extension of our formulation and numerical algorithms for pump–probe photoelectron spectroscopy to include the presence of nonadiabatic couplings. We then present several representative results of its application to wave packets on the nonadiabatically coupled ionic and covalent states in NaI to illustrate how energy- and angle-resolved pump–probe photoelectron spectra reflect the underlying wave packet dynamics in the nonadiabatic region where electron transfer occurs. Extensive results focusing on the more global behavior of the time-resolved photoelectron spectra in this system will be reported in a later paper. Since the principal aim of this paper is not a comparison of results with experiment, the effect of rotational motion on these spectra is not considered here but will be discussed elsewhere.

## II. FORMULATION

### A. Wave functions and equations of motion

Figure 1 illustrates the scheme used in our studies of pump–probe femtosecond photoelectron spectroscopy of vibrational wave packets on the nonadiabatically coupled ionic

a)Electronic mail: kaztak@mns2.c.u-tokyo.ac.jp
b)Electronic mail: mckoy@caltech.edu

 

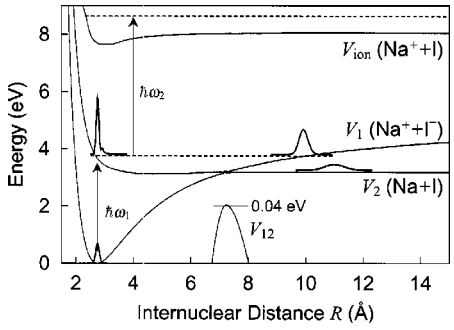


FIG. 1. NaI pump–probe photoelectron spectroscopy.

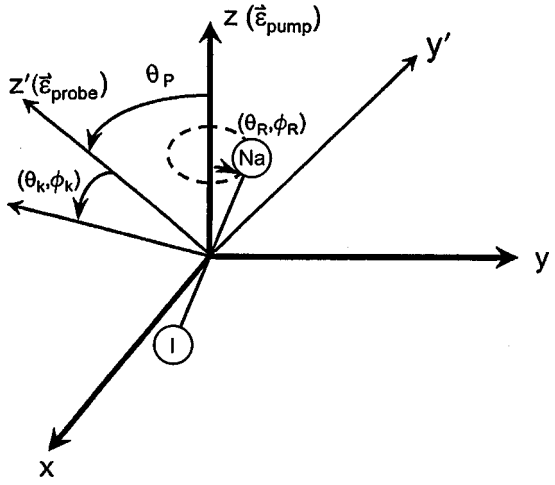


FIG. 2. Molecular orientation in the pump and probe coordinate systems.

and covalent states of NaI. A linearly polarized laser pulse of frequency $\omega_1$ prepares a wave packet on the lowest covalent state ($A\,^1\Sigma^+,\Omega=0^+$), which is ionized by a time-delayed linearly polarized pulse of frequency $\omega_2$. Figure 2 shows the relevant coordinate frames. The molecule is oriented at angles $(\theta_R,\phi_R)$ with respect to the polarization vector of the pump pulse, and the photoelectron angular distributions $(\theta_k,\phi_k)$ are measured relative to the polarization vector of the probe pulse. The angle between the probe and pump vectors is $\theta_P$ and, without loss of generality, the probe is assumed to lie in the $xz$ plane of the pump frame.

We begin with the Schrödinger equation

$$i\hbar\frac{\partial}{\partial t}\Psi(t)=[T_{\mathrm{N}}+H_{\mathrm{el}}+V(t)]\Psi(t), \tag{1}$$

where $T_{\mathrm{N}}$ is the nuclear kinetic energy operator and $H_{\mathrm{el}}$ is the electronic Hamiltonian. The interaction between the laser fields and molecule is given by

$$\begin{aligned}V(t)&=V_{\mathrm{pump}}(t)+V_{\mathrm{probe}}(t;\Delta T)\\&=E_{01}f_1(t)\sin(\omega_1 t)\boldsymbol{\varepsilon}_{\mathrm{pump}}\cdot\mathbf{d}\\&\quad+\frac{1}{2}E_{02}f_2(t-\Delta T)e^{-i\omega_2(t-\Delta T)}\boldsymbol{\varepsilon}_{\mathrm{probe}}\cdot\mathbf{d},\end{aligned} \tag{2}$$

where $V_{\mathrm{pump}}$ and $V_{\mathrm{probe}}$ represent the pump and probe fields, respectively, and, although more general forms can be readily assumed, we have made the rotating-wave approximation in $V_{\mathrm{probe}}$. $E_{01}$ and $E_{02}$ are the field amplitudes, $f_1(t)$ and $f_2(t-\Delta T)$ are Gaussian envelope functions, $\Delta T$ is the delay time between the two lasers, $\boldsymbol{\varepsilon}_{\mathrm{pump}}$ and $\boldsymbol{\varepsilon}_{\mathrm{probe}}$ are the polarization vectors, and $\mathbf{d}$ is the electric dipole operator. The pump pulse produces a polarized distribution of molecules with a $\cos^2(\theta_R)$ dependence with respect to $\boldsymbol{\varepsilon}_{\mathrm{pump}}$.[20] The time scale for rotation is generally two to three orders of magnitude slower than for vibrations and a probe laser with a pulse width of 40 fs is used to probe this aligned distribution of slowly rotating molecules.

The total wave function in the laboratory frame can be written as

$$\begin{aligned}\Psi(\mathbf{r},R,t)&=\chi_{\mathrm{g}}(R,t)\Phi_{\mathrm{g}}(\mathbf{r};R)+\chi_{\mathrm{e}}(R,t)\Phi_{\mathrm{e}}(\mathbf{r};R)\\&\quad+\int d\mathbf{k}\,\chi_{\mathbf{k}}(R,t)\Phi_{\mathbf{k}}^{(-)}(\mathbf{r};R),\end{aligned} \tag{3}$$

where $\Phi_{\mathrm{g}}$, $\Phi_{\mathrm{e}}$, and $\Phi_{\mathbf{k}}^{(-)}$ are eigenfunctions of $H_{\mathrm{el}}$ representing the ground, excited, and ion states, respectively, $\mathbf{r}$ denotes the electronic coordinates, and $R$ is the internuclear distance. Molecular rotation could be explicitly included in Eq. (3) by replacing $R$ with $\mathbf{R}$. The functions $\chi_{\mathrm{g}}$, $\chi_{\mathrm{e}}$, and $\chi_{\mathbf{k}}$ represent wave packets on the individual potential surfaces. Unlike excitation to a bound state, the final states in Eq. (3), $\chi_{\mathbf{k}}$, are characterized by a continuum of photoelectron energies and angles. The electronic functions $\Phi_{\mathrm{g}}$, $\Phi_{\mathrm{e}}$, and $\Phi_{\mathbf{k}}^{(-)}$ satisfy the equations

$$H_{\mathrm{el}}\Phi_{\mathrm{g}}(\mathbf{r};R)=V_{\mathrm{g}}(R)\Phi_{\mathrm{g}}(\mathbf{r};R), \tag{4}$$

$$H_{\mathrm{el}}\Phi_{\mathrm{e}}(\mathbf{r};R)=V_{\mathrm{e}}(R)\Phi_{\mathrm{e}}(\mathbf{r};R), \tag{5}$$

and

$$H_{\mathrm{el}}\Phi_{\mathbf{k}}^{(-)}(\mathbf{r};R)=\left[V_{\mathrm{ion}}(R)+\frac{(\hbar k)^2}{2m_e}\right]\Phi_{\mathbf{k}}^{(-)}(\mathbf{r};R), \tag{6}$$

where $m_e$ is the electron mass and the superscript $(-)$ on the continuum electronic wave function $\Phi_{\mathbf{k}}^{(-)}$ indicates incoming-wave boundary conditions, commonly used to represent dissociation (ejection) in stationary-state scattering theory. $V_{\mathrm{g}}(R)$, $V_{\mathrm{e}}(R)$, and $V_{\mathrm{ion}}(R)$ are the potential curves for the ground, excited, and ion states.

Projection of $\langle\Phi_{\mathrm{g}}|$, $\langle\Phi_{\mathrm{e}}|$, and $\langle\Phi_{\mathbf{k}}^{(-)}|$ onto the total Schrödinger equation (1) yields the following coupled equations of motion for the wave packets:

$$\begin{aligned}i\hbar\frac{\partial}{\partial t}\chi_{\mathrm{g}}(R,t)&=[T_{\mathrm{N}}+V_{\mathrm{g}}(R)]\chi_{\mathrm{g}}(R,t)+\langle\Phi_{\mathrm{g}}(R)|T_{\mathrm{N}}|\Phi_{\mathrm{e}}(R)\rangle\chi_{\mathrm{e}}(R,t)+\langle\Phi_{\mathrm{g}}(R)|V_{\mathrm{pump}}(t)|\Phi_{\mathrm{e}}(R)\rangle\chi_{\mathrm{e}}(R,t)\\&\quad+\int dk\sum_{lm}(-1)^m\langle\Phi_{\mathrm{g}}(R)|V_{\mathrm{probe}}(t)|\Phi_{kl-m}^{(-)}(R)\rangle\chi_{klm}(R,t),\end{aligned} \tag{7}$$

$$i\hbar\frac{\partial}{\partial t}\chi_e(R,t)=[T_N+V_e(R)]\chi_e(R,t)+\langle\Phi_e(R)|T_N|\Phi_g(R)\rangle\chi_g(R,t)+\langle\Phi_e(R)|V_{\text{pump}}(t)|\Phi_g(R)\rangle\chi_g(R,t)$$
$$+\int dk\sum_{lm}(-1)^m\langle\Phi_e(R)|V_{\text{probe}}(t)|\Phi^{(-)}_{kl-m}(R)\rangle\chi_{klm}(R,t), \tag{8}$$

and

$$i\hbar\frac{\partial}{\partial t}\chi_{klm}(R,t)=\left[T_N+V_{\text{ion}}(R)+\frac{(k\hbar)^2}{2m_e}\right]\chi_{klm}(R,t)+(-1)^m\langle\Phi^{(-)}_{kl-m}(R)|V_{\text{probe}}(t;\theta_R,\phi_R,\theta_P,\omega_2;\Delta T)|\Phi_g(R)\rangle\chi_g(R,t)$$
$$+(-1)^m\langle\Phi^{(-)}_{kl-m}(R)|V_{\text{probe}}(t;\theta_R,\phi_R,\theta_P,\omega_2;\Delta T)|\Phi_e(R)\rangle\chi_e(R,t), \tag{9}$$

where we have expanded $\Phi^{(-)}_{\mathbf{k}}$ and $\chi_{\mathbf{k}}$ in spherical harmonics, $Y_{lm}(\hat{k})$, and $\hat{k}$ is oriented with respect to the probe, i.e.,

$$\Phi^{(-)}_{\mathbf{k}}(\mathbf{r};R)=\sum_{lm}\Phi^{(-)}_{klm}(\mathbf{r};R)Y_{lm}(\hat{k}) \tag{10}$$

and

$$\chi_{\mathbf{k}}(R,t)=\sum_{lm}\chi_{klm}(R,t)Y_{lm}(\hat{k}). \tag{11}$$

The second term on the right-hand side of Eqs. (7) and (8) represents the nonadiabatic coupling between $\Phi_g(R)$ and $\Phi_e(R)$. In contrast to our previous studies of $Na_2$,[13] ionization of the ground state is possible and is represented by the last and second terms on the right-hand side of Eqs. (7) and (9), respectively. These coupled equations describe pump-probe ionization of wave packets which bifurcate and merge in the avoided crossing region.

### B. Matrix elements for excitation and photoionization

The procedures employed to obtain the requisite matrix elements for optical excitation and photoionization have been discussed previously.[13] Here we will only outline a few essential features. The dipole interaction between the ground and excited states is

$$V_{\text{eg}}=\langle\Phi_e|V_{\text{pump}}(t)|\Phi_g\rangle$$
$$=-E_{01}f_1(t)\sin(\omega_1 t)d_{\text{eg}}\cos(\theta_R), \tag{12}$$

where $d_{\text{eg}}$ is the magnitude of the dipole transition moment. Hence, in a sufficiently weak field where Rabi oscillation is suppressed, the distribution of molecular orientation in the excited state is proportional to $\cos^2(\theta_R)$.

The photoionization matrix elements are a key quantity in these studies. To obtain these matrix elements, we assume a frozen-core Hartree–Fock description for the final ionized state in which $\Phi^{(-)}_{\mathbf{k}}$ is written as an antisymmetrized product of a Hartree–Fock ion core wave function $\Phi_+$ and a photoelectron orbital $\phi^{(-)}_{\mathbf{k}}$,

$$\Phi^{(-)}_{\mathbf{k}}=\mathcal{A}(\Phi_+\cdot\phi^{(-)}_{\mathbf{k}}). \tag{13}$$

While extensive configuration-interaction (CI) wave functions are essential for a robust representation of the ground and excited states, $\Phi_g$ and $\Phi_e$, where there are avoided crossings, the Hartree–Fock model provides an adequate representation of the ionic state over all internuclear distances of interest. The coupling matrix element between the excited state $\Phi_e$ (or $\Phi_g$) and the ionized state can be written as

$$\langle\Phi^{(-)}_{\mathbf{k}}(R)|V_{\text{probe}}(t;\Delta T)|\Phi_e(R)\rangle$$
$$=\frac{1}{2}E_{02}f_2(t-\Delta T)\exp[-i\omega_2(t-\Delta T)]\sum_{lm}C_{e,lm}Y_{lm}(\hat{k}) \tag{14}$$

and

$$C_{e,lm}(R;k,\theta_R,\phi_R,\theta_P)=\sqrt{\frac{4\pi}{3}}\sum_{\lambda\mu}I_{l\lambda\mu}\mathcal{D}^{l*}_{\lambda m}(\hat{R}')\mathcal{D}^{1}_{\mu\mu_0}(\hat{R}'), \tag{15}$$

where $\hat{R}'$ specifies the angles of the probe frame with respect to the body frame (Fig. 2). $I_{l\lambda\mu}$ is a matrix element of the dipole operator between the excited state CI wave function and $|\Phi_+\psi^{(-)}_{kl\lambda}\rangle$,[13,15] where $\psi^{(-)}_{kl\lambda}$ is a partial-wave component of $\phi^{(-)}_{\mathbf{k}}$ in the molecular frame, i.e.,

$$\phi^{(-)}_{\mathbf{k}}=\sum_{lm\lambda}i^l e^{-i\eta_l}\mathcal{D}^{l}_{\lambda m}(\hat{R}')Y^*_{lm}(\hat{k})\psi^{(-)}_{kl\lambda}(\mathbf{r}';R). \tag{16}$$

In Eq. (16), $\lambda$ is the projection of $l$ in the body frame and $\eta_l$ is the Coulomb phase shift. The procedures employed to obtain the $\psi^{(-)}_{kl\lambda}$'s numerically are discussed in Ref. 21. The corresponding coefficients for ionization of the ground state, $C_{g,lm}$, are constructed with a similar procedure.

With these coupling matrix elements, the equations of motion for the nuclear wave packets can be written as

$$i\hbar\frac{\partial}{\partial t}\chi_g(R,t)=[T_N+V_g(R)]\chi_g(R,t)+V_{ge}(R)\chi_e(R,t)$$
$$+T_{ge}(R)\chi_e(R,t)+\frac{1}{2}\int dkk^2\sum_{lm}E_{02}$$
$$\times f_2(t-\Delta T)\exp[i\omega_2(t-\Delta T)]$$
$$\times C^*_{g,lm}(R;k,\theta_R,\phi_R,\theta_P)\chi_{klm}(R,t), \tag{17}$$

$$i\hbar\frac{\partial}{\partial t}\chi_e(R,t)=[T_N+V_e(R)]\chi_e(R,t)+V_{eg}(R)\chi_g(R,t)$$
$$+T_{eg}(R)\chi_g(R,t)+\frac{1}{2}\int dkk^2\sum_{lm}E_{02}$$
$$\times f_2(t-\Delta T)\exp[i\omega_2(t-\Delta T)]$$
$$\times C^*_{e,lm}(R;k,\theta_R,\phi_R,\theta_P)\chi_{klm}(R,t), \tag{18}$$

and

$$i\hbar\frac{\partial}{\partial t}\chi_{klm}(R,t)=\left[T_{\mathrm{N}}+V_{\mathrm{ion}}(R)+\frac{(k\hbar)^2}{2m_e}\right]\chi_{klm}(R,t)$$
$$+\frac{1}{2}E_{02}f_2(t-\Delta T)\exp[-i\omega_2(t-\Delta T)]$$
$$\times C_{\mathrm{g},lm}(R;k,\theta_R,\phi_R,\theta_P)\chi_{\mathrm{g}}(R,t)$$
$$+\frac{1}{2}E_{02}f_2(t-\Delta T)\exp[-i\omega_2(t-\Delta T)]$$
$$\times C_{\mathrm{e},lm}(R;k,\theta_R,\phi_R,\theta_P)\chi_{\mathrm{e}}(R,t). \quad (19)$$

### C. Transformation from adiabatic to diabatic representation

In spite of the impressive advances in computational methodologies for molecular electronic structure calculations, obtaining nonadiabatic coupling matrix elements with highly correlated electronic wave functions remains challenging. Furthermore, photoionization amplitudes must also now be determined with such correlated wave functions. We have hence employed the following strategy to address these difficulties in the nonadiabatic region.

We designate the adiabatic potentials explicitly as $V_{\mathrm{g}}^{\mathrm{a}}$ and $V_{\mathrm{e}}^{\mathrm{a}}$. We then construct diabatic surfaces $V_1^{\mathrm{d}}(R)$ and $V_2^{\mathrm{d}}(R)$ globally with a smooth interpolation of $V_{\mathrm{g}}^{\mathrm{a}}(R)$ and $V_{\mathrm{e}}^{\mathrm{a}}(R)$ such that

$$V_1^{\mathrm{d}}(R)=V_{\mathrm{g}}^{\mathrm{a}}(R),\quad V_2^{\mathrm{d}}(R)=V_{\mathrm{e}}^{\mathrm{a}}(R), \quad (20)$$

for $R\ll R_{\mathrm{X}}$, and

$$V_1^{\mathrm{d}}(R)=V_{\mathrm{e}}^{\mathrm{a}}(R),\quad V_2^{\mathrm{d}}(R)=V_{\mathrm{g}}^{\mathrm{a}}(R), \quad (21)$$

for $R\gg R_{\mathrm{X}}$, where $R_{\mathrm{X}}$ is the crossing point, defined as the point where $V_{\mathrm{e}}^{\mathrm{a}}(R)-V_{\mathrm{g}}^{\mathrm{a}}(R)$ is a minimum. Furthermore, to connect the diabatic curves smoothly, we impose the natural condition

$$V_1^{\mathrm{d}}(R_{\mathrm{X}})=V_2^{\mathrm{d}}(R_{\mathrm{X}})=\frac{1}{2}[V_{\mathrm{g}}^{\mathrm{a}}(R_{\mathrm{X}})+V_{\mathrm{e}}^{\mathrm{a}}(R_{\mathrm{X}})]. \quad (22)$$

Interpolation through the crossing region to obtain the diabatic potentials was found to be quite stable and to depend little on the choice of algorithm and range of interpolation. We can then write the matrix of the electronic Hamiltonian in the diabatic representation as

$$\langle\Phi_i^{\mathrm{d}}(R)|H_{\mathrm{el}}|\Phi_j^{\mathrm{d}}(R)\rangle=\begin{pmatrix}V_1^{\mathrm{d}}(R) & V_{12}(R)\\ V_{21}(R) & V_2^{\mathrm{d}}(R)\end{pmatrix}, \quad (23)$$

where $V_{21}(R)$ and $V_{12}(R)$ are not yet known. Within the two-level approximation, diagonalization of this matrix with an orthogonal matrix $U(R)$,

$$U(R)=\begin{pmatrix}\cos\Omega(R) & \sin\Omega(R)\\ -\sin\Omega(R) & \cos\Omega(R)\end{pmatrix}, \quad (24)$$

yields the adiabatic representation of $H_{\mathrm{el}}$, i.e.,

$$U^{-1}(R)\begin{pmatrix}V_1^{\mathrm{d}}(R) & V_{12}(R)\\ V_{12}(R) & V_2^{\mathrm{d}}(R)\end{pmatrix}U(R)$$
$$=\begin{pmatrix}V_{\mathrm{g}}^{\mathrm{a}}(R) & 0\\ 0 & V_{\mathrm{e}}^{\mathrm{a}}(R)\end{pmatrix}. \quad (25)$$

The two independent linear equations implied by Eqs. (25) permit determination of the parameter $\Omega(R)$ in $U(R)$ and the coupling element $V_{12}(R)$ at each $R$. In this way, we obtain the diabatic potential surfaces, their coupling elements, and the transformation matrix $U(R)$. This transformation matrix is then used to transform the photoionization amplitudes from the adiabatic to diabatic surfaces

$$\begin{pmatrix}C_{1,lm}(R;k,\theta_R,\phi_R,\theta_P)\\ C_{2,lm}(R;k,\theta_R,\phi_R,\theta_P)\end{pmatrix}$$
$$=U(R)\begin{pmatrix}C_{\mathrm{g},lm}(R;k,\theta_R,\phi_R,\theta_P)\\ C_{\mathrm{e},lm}(R;k,\theta_R,\phi_R,\theta_P)\end{pmatrix}, \quad (26)$$

as well as the matrix element for the pump laser, $\langle\Phi_{\mathrm{e}}(R)|V_{\mathrm{pump}}(t)|\Phi_{\mathrm{g}}(R)\rangle$, to the diabatic basis $\langle\Phi_2^{\mathrm{d}}(R)|V_{\mathrm{pump}}(t)|\Phi_1^{\mathrm{d}}(R)\rangle$.

### D. Solution of coupled equations

To solve the equations of motion in the diabatic representation, we further discretize the integral over $k$ to obtain

$$i\hbar\frac{\partial}{\partial t}\chi_1(R,t)=[T_{\mathrm{N}}+V_1^{\mathrm{d}}(R)]\chi_1(R,t)+V_{12}(R)\chi_2(R,t)$$
$$+\frac{1}{2}\sum_j w_j k_j^2\sum_{lm}E_{02}$$
$$\times f_2(t-\Delta T)\exp[i\omega_2(t-\Delta T)]$$
$$\times C_{1,lm}^*(R;k_j,\theta_R,\phi_R,\theta_P)\chi_{k_j lm}(R,t), \quad (27)$$

$$i\hbar\frac{\partial}{\partial t}\chi_2(R,t)=[T_{\mathrm{N}}+V_2^{\mathrm{d}}(R)]\chi_2(R,t)+V_{21}(R)\chi_1(R,t)$$
$$+\frac{1}{2}\sum_j w_j k_j^2\sum_{lm}E_{02}$$
$$\times f_2(t-\Delta T)\exp[i\omega_2(t-\Delta T)]$$
$$\times C_{2,lm}^*(R;k_j,\theta_R,\phi_R,\theta_P)\chi_{k_j lm}(R,t), \quad (28)$$

and

$$i\hbar\frac{\partial}{\partial t}\chi_{k_j lm}(R,t)=\left[T_{\mathrm{N}}+V_{\mathrm{ion}}(R)+\frac{(k_j\hbar)^2}{2m_e}\right]\chi_{k_j lm}(R,t)$$
$$+\frac{1}{2}E_{02}f_2(t-\Delta T)\exp[-i\omega_2(t-\Delta T)]$$
$$\times C_{1,lm}(R;k_j,\theta_R,\phi_R,\theta_P)\chi_1(R,t)$$
$$+\frac{1}{2}E_{02}f_2(t-\Delta T)\exp[-i\omega_2(t-\Delta T)]$$
$$\times C_{2,lm}(R;k_j,\theta_R,\phi_R,\theta_P)\chi_2(R,t), \quad (29)$$

where $N_k$ is the number of quadrature points and $w_j$ the associated weights. To make the Hamiltonian matrix for these coupled equations Hermitian, we work with the quantities

$$\tilde{\chi}_{k_j lm}(R,t) = k_j \sqrt{w_j}\chi_{k_j lm}(R,t), \tag{30}$$

$$\tilde{C}_{1,lm}(R;k_j,\theta_R,\phi_R,\theta_P) = k_j \sqrt{w_j} C_{1,lm}(R;k_j,\theta_R,\phi_R,\theta_P), \tag{31}$$

and $\tilde{C}_{2,lm}$ as well. A treatment without this Hermitization destabilizes the numerical calculations.

The solution of these coupled equations can be written as a vector $\boldsymbol{\chi}$,

$$\boldsymbol{\chi}(R,t) = \begin{pmatrix} \chi_1(R,t) \\ \chi_2(R,t) \\ \vdots \\ \tilde{\chi}_{k_j lm}(R,t) \\ \vdots \end{pmatrix}, \tag{32}$$

which can typically contain several hundred or more components. The coupled equations of motion for the nuclear wavepackets is now written in matrix form as

$$i\hbar \frac{\partial}{\partial t}\boldsymbol{\chi}(R,t) = \mathbf{H}(R,t)\boldsymbol{\chi}(R,t) = [\mathbf{T} + \mathbf{V}_{\mathrm{D}}(R) + \mathbf{V}_{\mathrm{NA}}(R) + \mathbf{V}_{\mathrm{pump}}(R,t) + \mathbf{V}_{\mathrm{probe}}(R,t)]\boldsymbol{\chi}(R,t), \tag{33}$$

where $\mathbf{T}$ is a diagonal matrix representing the kinetic energy operator:

$$\mathbf{T} = \begin{pmatrix} T_{\mathrm{N}} & 0 & 0 & & \\ 0 & T_{\mathrm{N}} & 0 & & \\ 0 & 0 & T_{\mathrm{N}} & & \\ & & & \ddots & \end{pmatrix}. \tag{34}$$

$\mathbf{V}_{\mathrm{D}}(R)$ is a diagonal matrix of potential energy surfaces for the ground, excited, and ionized states,

$$\mathbf{V}_{\mathrm{D}}(R) = \begin{pmatrix} V_1(R) & 0 & 0 & & \\ 0 & V_2(R) & 0 & 0 & \\ 0 & 0 & V_{\mathrm{ion}}(R) + \dfrac{(k_1\hbar)^2}{2m_e} & & \\ & 0 & & V_{\mathrm{ion}}(R) + \dfrac{(k_2\hbar)^2}{2m_e} & \\ & 0 & & & \ddots \end{pmatrix}, \tag{35}$$

and $\mathbf{V}_{\mathrm{NA}}(R)$ represents the nonadiabatic interaction:

$$\mathbf{V}_{\mathrm{NA}}(R) = \begin{pmatrix} 0 & V_{12}(R) & 0 & \\ V_{21}(R) & 0 & 0 & \\ 0 & 0 & 0 & \\ & & & \ddots \end{pmatrix}. \tag{36}$$

In Eqs. (35) and (36) and below, we omit the superscript "d" on the potentials and electronic wave functions, e.g., $V_1^{\mathrm{d}}(R)$ and $\Phi_1^{\mathrm{d}}(R)$. $\mathbf{V}_{\mathrm{pump}}(R,t)$ is the pump–laser interaction,

$$\mathbf{V}_{\mathrm{pump}}(R,t) = \begin{pmatrix} 0 & \langle\Phi_2(R)|V_{\mathrm{pump}}(t)|\Phi_1(R)\rangle & 0 & \\ \langle\Phi_1(R)|V_{\mathrm{pump}}(t)|\Phi_2(R)\rangle & 0 & 0 & \\ 0 & 0 & 0 & \\ & & & \ddots \end{pmatrix}, \tag{37}$$

while $\mathbf{V}_{\mathrm{probe}}(R,t)$ represents the probe–laser interaction,

$$\mathbf{V}_{\mathrm{probe}}(R,t) = \frac{1}{2}E_{02}f_2 \exp[-i\omega_2(t-\Delta T)] \begin{pmatrix} 0 & 0 & \cdots & \tilde{C}_{1,lm} & \cdots \\ 0 & 0 & \cdots & \tilde{C}_{2,lm} & \cdots \\ \vdots & \vdots & & & \\ \tilde{C}^*_{1,lm} & \tilde{C}^*_{2,lm} & & 0 & \\ \vdots & \vdots & \ddots & & \end{pmatrix}, \tag{38}$$

where, for brevity, we omit the arguments in $\tilde{C}_{1,lm}$ and $\tilde{C}_{2,lm}$.

Defining

$$\mathbf{V}_{\mathrm{O}}(R,t) = \mathbf{V}_{\mathrm{NA}}(R) + \mathbf{V}_{\mathrm{pump}}(R,t) + \mathbf{V}_{\mathrm{probe}}(R,t), \tag{39}$$

the coupled equations of motion can be solved with split-operator techniques. The formal solution is approximated by

$$\begin{aligned}\boldsymbol{\chi}(R,t+\Delta t) &\simeq \exp\left(-\frac{i\Delta t}{\hbar}\mathbf{H}(R,t)\right)\boldsymbol{\chi}(R,t)\\ &\simeq \exp\left(-\frac{i\Delta t}{2\hbar}[\mathbf{T}(R)+\mathbf{V}_{\mathrm{D}}(R)]\right)\exp\left(-\frac{i\Delta t}{\hbar}\mathbf{V}_{\mathrm{O}}(R,t)\right)\exp\left(-\frac{i\Delta t}{2\hbar}[\mathbf{T}(R)+\mathbf{V}_{\mathrm{D}}(R)]\right)\chi(R,t)\\ &\simeq \exp\left(-\frac{i\Delta t}{4\hbar}\mathbf{V}_{\mathrm{D}}(R)\right)\exp\left(-\frac{i\Delta t}{2\hbar}\mathbf{T}(R)\right)\exp\left(-\frac{i\Delta t}{4\hbar}\mathbf{V}_{\mathrm{D}}(R)\right)\\ &\quad\times\exp\left(-\frac{i\Delta t}{\hbar}\mathbf{V}_{\mathrm{O}}(R,t)\right)\exp\left(-\frac{i\Delta t}{4\hbar}\mathbf{V}_{\mathrm{D}}(R)\right)\exp\left(-\frac{i\Delta t}{2\hbar}\mathbf{T}(R)\right)\exp\left(-\frac{i\Delta t}{4\hbar}\mathbf{V}_{\mathrm{D}}(R)\right)\boldsymbol{\chi}(R,t).\end{aligned} \tag{40}$$

Various techniques employed in solving these equations including the quadrature over $k$, fast Fourier transforms (FFTs), and symplectic integration of the wave packet are essentially similar to those used in our previous study on $Na_2$.[13]

## III. APPLICATION TO NaI

The seminal studies of Zewail and co-workers established NaI as a benchmark system for monitoring wave packet motion.[22–24] In these experiments a femtosecond pump laser launches a wave packet on the covalent excited state which is coupled nonadiabatically to the ground state (Fig. 1). The wave packet oscillates across the adiabatic potential well formed by the avoided crossing of the covalent (NaI) state and ionic ($Na^+I^-$) states. In the region of the avoided crossing an electron is transferred from Na to I and the bond converts from covalent to ionic. In these studies,[22–24] the time evolution of the wave packet was monitored by excitation to a higher state and fluorescence from this state. More recently, Jouvet *et al.*[6] have followed the wave packet evolution on the same state of NaI by time-resolved detection of photoelectron energy distributions and photoions. These photoelectron spectra and ion energy distributions provided valuable insight into the nuclear dynamics of this system. There have also been several theoretical studies of the pump–probe photoelectron energy distributions[17,25] and of dissociative ionization[25] of this same state of NaI. While the early studies of this system by Engel and co-workers[17] did not include any dependence of the photoionization amplitude on geometry, Charron and Suzor-Weiner[25] employed an empirical form to account for the change in the transition dipole as the wave packet moved from the covalent to ionic regions and obtained photoelectron and photoion spectra in good agreement with the measurements of Ref. 6. Such $R$ dependence of the photoionization amplitude has also been observed to be essential in accounting for the unexpected inward–outward asymmetry in femtosecond two-photon ionization of wave packets on the A state of NaI.[26]

Here we report results of calculations of the energy and angular distributions of photoelectrons from wave packets on these coupled covalent and ionic states of NaI. A key objective of these studies is to explore the potential of energy- and angle-resolved pump-probe photoelectron spectra for probing the intramolecular electron transfer occurring between the covalent and ionic states ($NaI \rightarrow Na^+I^-$) in the nonadiabatic region. Our pump (3.73 eV) and probe (4.89 eV) photon energies, which differ from the pump (3.97 eV) and probe (4.71 eV) energies of Refs. 6 and 25, are well suited for probing the wave packet motion across the avoided crossing and are chosen with this in mind. To account for the dependence of the photoionization amplitude on internuclear distance in this system, particularly in the crossing region, geometry-dependent amplitudes are employed in these calculations. Further details of these cross sections and their dependence on geometry and energy will be discussed elsewhere. Here we only comment briefly on a few salient and relevant features. The cross sections for ionization of the wave packet on the ionic branch of the excited state are expectedly much larger than on the inner (covalent) well and depend quite strongly on energy and distance. They range in value between 15 and 30 Mb and continue to show molecularlike behavior out to the turning point (10 Å), reflecting the ion-pair character of the state. In contrast, the cross section on the covalent branch can be of the order of 1–3 Mb, which is significantly larger than the cross section for the sodium atom (~0.1 Mb). This difference reflects the molecular nature of the covalent (NaI) state.

### A. Potential surfaces

The adiabatic potential energy surfaces for the ground, excited, and ion states were obtained from high-level electronic structure calculations using the MOLPRO code. It was still necessary, however, to shift the neutral potential curves slightly to adjust the excitation energy to the experimental values and the final value of the nonadiabatic coupling matrix element (see Fig. 1). It is worth noting that it was also essential to include spin–orbit interaction to correctly describe the covalent potential curve in the region where the wave packet is launched. Further details including a discussion of the photoionization matrix elements $C_{lm}$ and their behavior with distance will be presented in a future publication.[27]

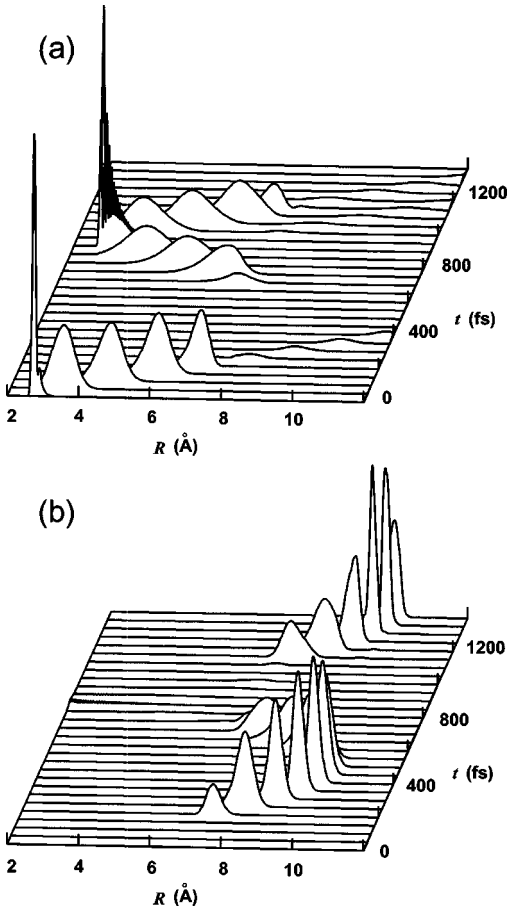


FIG. 3. Pump-pulse excited wave packet motion on the diabatic states, (a) $V_1$ (ionic) and (b) $V_2$ (covalent).

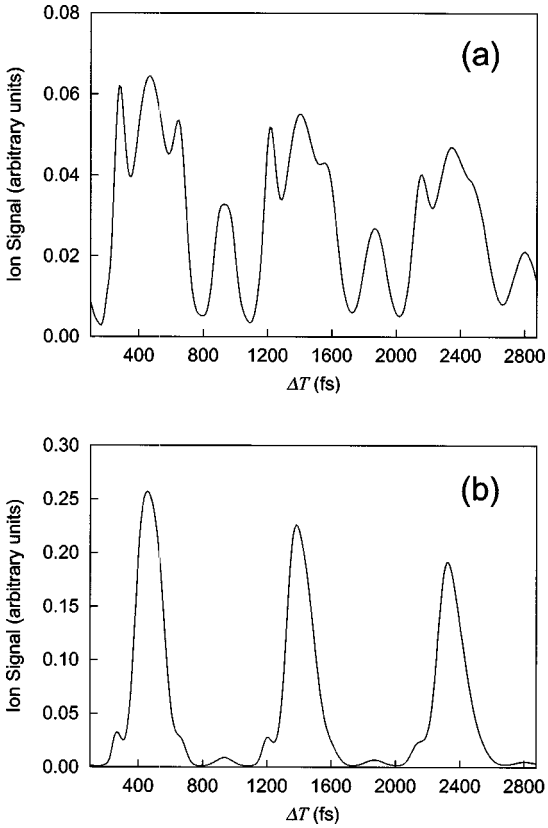


FIG. 4. Total ion signals vs pump–probe delay time. Probe polarization (a) parallel and (b) perpendicular to the pump polarization.

### B. Wave packet motion

Figure 3 shows the wave packets on the ionic ($V_1$, lower panel) and covalent ($V_2$, upper panel) diabatic states for a linearly polarized pump pulse of 3.73 eV with a full width at half maximum (FWHM) of 40 fs and centered at $t=0$. These diabatic potentials provide a very pictorial view of the wave packet motion on these nonadiabatically coupled surfaces. After launching, the wave packet moves to the right and undergoes bifurcation at the crossing point between $V_1$ and $V_2$. The component of the wave packet that continues along $V_2$ represents dissociation into neutral atoms. The component moving on the ionic surface reaches its right-hand turning point near 10 Å at around 475 fs. This component returns to the crossing point at around 725 fs and bifurcates. The component on the $V_2$ (covalent) surface reaches the left-hand turning point at ~925 fs.

### C. Total photoelectron signal

For ionization of these wave packets we choose a probe pulse with a photon energy of 4.89 eV which is just sufficient for ionization of the wave packet on $V_2$ (covalent) beyond the crossing point. This pulse has a FWHM of 40 fs and its polarization can be either parallel or perpendicular to the molecular axis.

The total ion signal for a pump–probe delay time $\Delta T$ is given by

$$P_{\text{total}}(\Delta T) = \int d\mathbf{k} \int dR |\chi_{\mathbf{k}}(R,t_f;\Delta T)|^2$$
$$= \int dk k^2 \sum_{lm} \int dR |\chi_{klm}(R,t_f;\Delta T)|^2$$
$$= \int P_{\text{total}}(\varepsilon_k;\Delta T) d\varepsilon_k, \tag{41}$$

where $t_f$ is a time sufficiently long after the probe pulse interaction is over. Figure 4(a) shows the total ion signal for the polarization vectors of the pump and probe lasers parallel to the molecular axis. The peaks centered around 400, 1350, and 2300 fs arise from ionization of the wavepackets at the right-hand turning point on the ionic surface while those around 900, 1850, and 2800 fs are due to wave packets located at the left-hand turning point on the $V_2$ covalent surface. The shape of the ion signal at the right-hand turning point (400, 1350, and 2300 fs) reflects the slowing down of the wave packet there and the dependence of $C_{1,lm}$ on $R$. The valleys between peaks for ionization at the right- and left-hand turning points—e.g., $\Delta T=800$ fs—indicate passage of the wave packet through the avoided crossing region. The decreasing height of these peaks with delay time results from loss of NaI population to dissociation.

The ion signal with the probe polarization perpendicular to the molecular axis [Fig. 4(b)] is significantly larger than for the parallel alignment. The shapes of these ion signals for parallel and perpendicular orientation of the polarization of probe laser to the molecular axis reflect differences in the

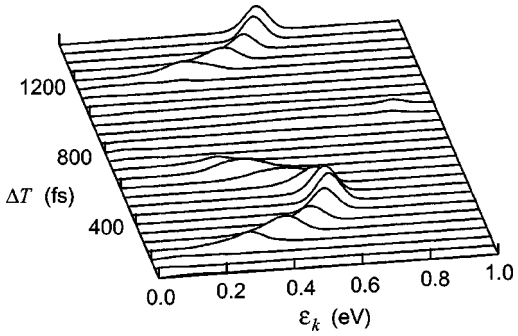


FIG. 5. Photoelectron kinetic energy distributions vs delay time $\Delta T$. Probe polarization parallel to that of the pump.

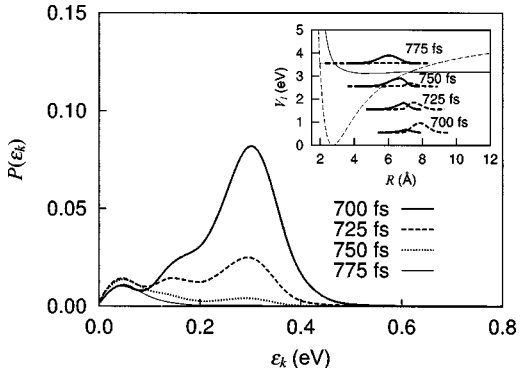


FIG. 7. Photoelectron energy spectrum as the wave packet transfers from the ionic to the covalent curve (second crossing).

behavior of the photoionization amplitudes with $R$. The perpendicular signal is dominated by ionization of the wave packet from the region around the right-hand turning point.

### D. Photoelectron kinetic energy distributions

Figure 5 shows the photoelectron energy distributions as a function of pump–probe delay time with the probe polarization parallel to the molecular axis. As seen in previous studies of this system,[17,25] the kinetic energy distributions map the vibrational wave packet motion quite nicely: the photoelectron energy increases as the wave packet moves to the right on the covalent state, bifurcates at the crossing point, climbs up the ionic potential, and reaches its turning point around 475 fs where the photoelectron energy is about 0.6 eV. The much weaker peak at 0.8 eV and 900 fs maps the wave packet near the left-hand turning point on the covalent state. The very low photoelectron signal between pump–probe delays of ~750 fs and 1150 fs, when the wave packet is on the covalent state, reflects the vast difference in the amplitudes for ionization on the covalent and ionic states.[27]

We now look more closely at how these photoelectron energy distributions map the motion of the wave packet in the crossing region. Figure 6 shows the photoelectron spectra for pump–probe delays of 175, 200, 225, and 250 fs. Snapshots of the wave packets on the diabatic potentials are also shown as insets in this figure. At 175 fs the single peak around 0.1 eV in the photoelectron spectrum and its low intensity are signatures of the wave packet on the covalent potential. By 200 fs the wave packet has bifurcated, resulting in components on the covalent and ionic potentials which give rise to peaks in the photoelectron spectrum ~0.1 eV and 0.3 eV, respectively. The peak at 0.3 eV reflects the greater kinetic energy available to photoelectrons from the wave packet on the ionic potential than from the wave packet on the covalent potential. By 225 fs continued bifurcation onto the ionic potential leads to a dominant peak at 0.3 eV and a weak shoulder to lower energy in the photoelectron spectrum. At 250 fs the spectrum has evolved into a strong feature around 0.3 eV in the spectrum arising from the wave packet on the ionic potential. The near 15-fold larger intensity of the peak at 0.3 eV (250 fs) over the peak at 0.1 eV (175 fs) is a result of the much greater magnitude of the photoionization amplitude for the ionic state than for the covalent state. The photoelectron signal from the wave packet on the covalent potential beyond the crossing point is expected to be negligible.

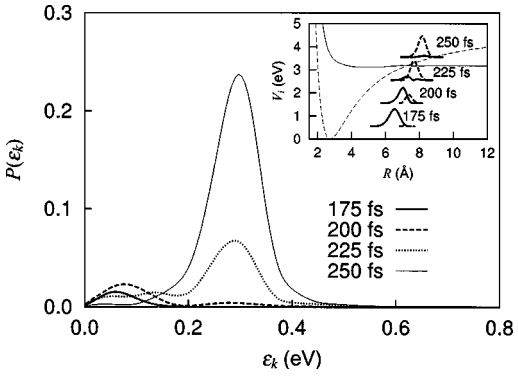


FIG. 6. Photoelectron energy spectrum as the wave packet bifurcates at the avoided crossing (first crossing). The probe polarization is perpendicular to that of the pump in Figs. 6 and 7.

As a second example, we look at the photoelectron spectra for the wave packet as it moves back down on the ionic potential and begins to reenter the crossing region. Figure 7 shows these spectra for pump–probe delays of 700, 725, 750, and 775 fs. The evolution of these spectra with pump–probe delay again illustrates how the photoelectron energy distributions map the motion of the wave packet through the crossing region. In contrast to the previous example where the wave packet was bifurcating onto the ionic potential, here the photoelectron signal decreases with delay time as the wave packet moves onto the covalent potential where the photoionization amplitude is smaller.

As a final example, Fig. 8 shows photoelectron spectra with the probe polarization parallel to the molecular axis for pump–probe delays of 1600, 1675, 1700, and 1725 fs when the wave packet is reentering the crossing region for the second time from the ionic potential. The evolution of the lower- and higher-energy peaks in the spectra with time is seen to monitor the bifurcation of the wave packet through the avoided crossing region. The broadening of the energy distribution at 1700 and 1725 fs to higher energy is due to greater spreading of the wave packet on the covalent potential at these times than at the first crossing—e.g., 775 fs. These and other features of these spectra will be discussed in a future publication.[27]

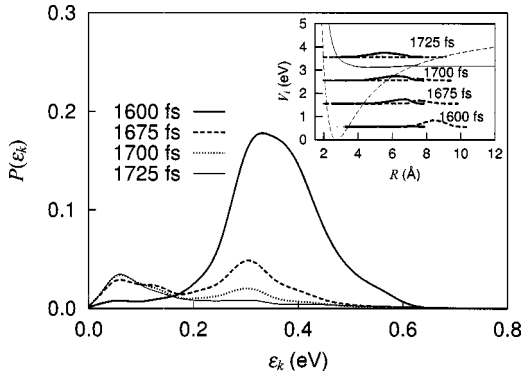


FIG. 8. Photoelectron energy spectrum as the wave packet moves from the ionic onto the covalent curve (fourth crossing).

### E. Photoelectron angular distributions

The angular distribution of the photoelectrons is given by

$$A(\theta_k,\Delta T,\varepsilon_k)=\int dR\left|\sum_{\ell m}\chi_{klm}(R,t_f,\Delta T)\times Y_{lm}(\theta_k,\phi_k=0)\right|^2 k, \tag{42}$$

where the angles $(\theta_k,\phi_k)$ are in the laboratory frame (Fig. 2). For convenience, we transform these distributions to the molecular frame to facilitate comparison of the angular distributions for parallel and perpendicular orientations of the polarization of the probe laser to the molecular axis.

We now explore a few examples of these angular distributions to see how they may reflect intramolecular electron transfer between the covalent and ionic states—i.e., NaI $\rightarrow Na^+ + I^-$—in the crossing region. We will report on these angular distributions more broadly in a future publication.[27] Figure 9 (upper panel) shows the angular distribution of photoelectrons with 0.05 eV, the peak energy in the spectrum, for photoionization of the wave packet at a pump–probe delay of 125 fs. In this figure the sodium and iodine ends of the molecule are at 0° and 180°, respectively. The peaking of the distribution at lower angles (~20°) implies that ionization of the wave packet on the covalent surface to the left of the crossing (see lower right panel) favors ejection of electrons from the sodium side. This behavior is also observed at other photoelectron energies in the spectrum—e.g., 0.13 and 0.3 eV. This can also be seen in the polar plot of the angular distribution, integrated over kinetic energy, shown in the lower left frame of Fig. 9.

Figure 10 shows the angular distribution of photoelectrons at 0.08 eV, the peak energy in the spectrum, for photoionization at a pump–probe delay of 175 fs when the wave packet has moved into the crossing region. Electrons are now preferentially ejected from the iodine side of the molecule, reflecting the increasing ionic character of the wave packet as the electron transfers from sodium to iodine—i.e., NaI $\rightarrow Na^+ + I^-$. This same behavior is seen in the angular distributions, integrated over kinetic energy, in Fig. 10. By 225 fs the wave packet has moved to the right of the crossing (Fig. 10) and the angular distribution continues to favor electron ejection from the iodine ($I^-$) side of the molecule. The evolution of these angular distributions as the wave packet moves from the covalent (NaI) to ionic ($Na^+I^-$) potentials suggests that such spectra can be a useful window on the real-time dynamics of electron transfer.

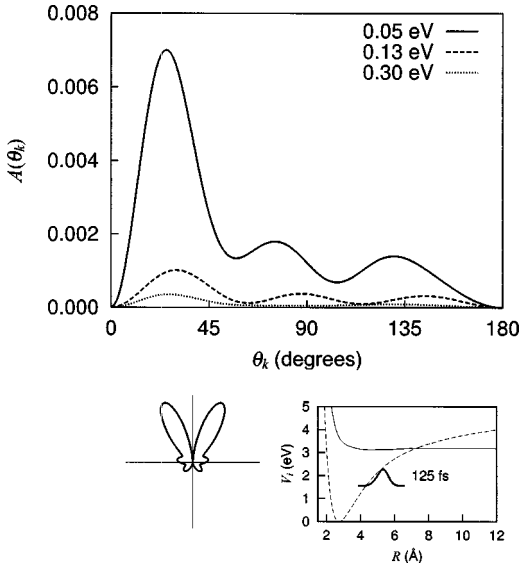


FIG. 9. Photoelectron angular distributions at delay time $\Delta T=125$ fs (upper panel). Polar plot of the energy-integrated photoelectron angular distribution for the same delay time (lower left panel). (Sodium lies at the top of the vertical axis in the polar plots in Figs. 9–12.) Wave packet snapshot (lower right panel). Probe polarization perpendicular to that of the pump.

Figure 11 tracks the evolution of the angular distribution of photoelectrons as the wave packet enters the crossing region on its way back from the right-hand turning point. The frames at 700, 750, and 800 fs show the energy-integrated angular distributions as they evolve from two dominant lobes

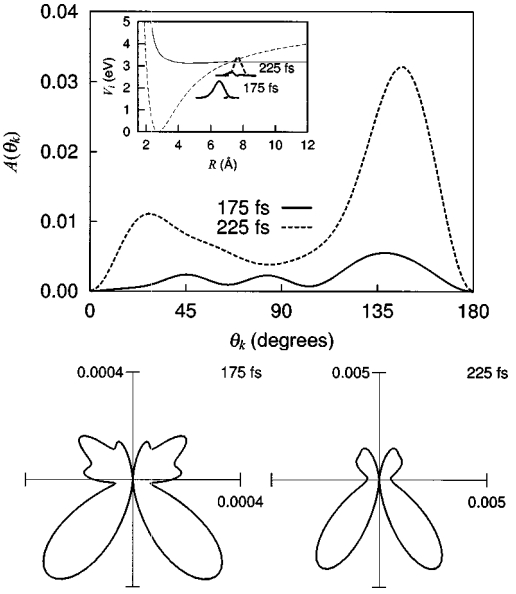


FIG. 10. Photoelectron angular distributions at peak energy (0.08 eV for 175 fs and 0.30 eV for 225 fs) of each photoelectron spectrum (upper panel) and wave packet snapshots at corresponding delay times (inset). Energy-integrated photoelectron angular distributions (lower panel). Probe polarization perpendicular to that of the pump.

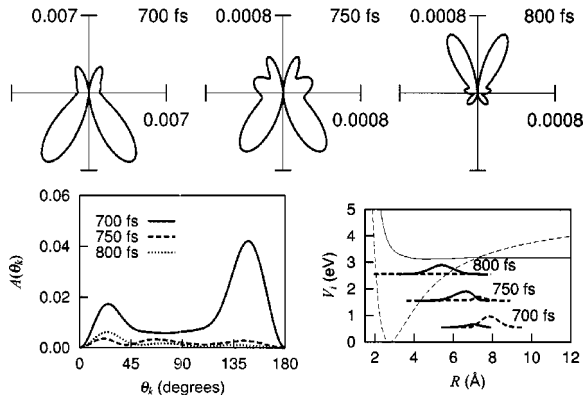


FIG. 11. Energy-integrated photoelectron angular distributions as the wave packet transfers from the ionic to the covalent curve (upper panel). Photoelectron angular distributions at peak energy (0.30 eV for 700 fs, 0.05 eV for 750 and 800 fs) of each photoelectron spectrum (lower left panel). Wave packet snapshots at corresponding delay times (lower right panel). Probe polarization perpendicular to that of the pump.

towards the iodine end of the molecule at 700 fs, where the wave packet is essentially on the ionic state ($Na^+I^-$), to two dominant lobes towards the sodium end of the molecule at 800 fs when the wave packet is on the covalent state (NaI). The angular distribution at 750 fs displays features transitional between those at 700 and 800 fs. The tenfold decrease in intensity of the distributions from 700 to 800 fs again reflects the much larger magnitude of the photoionization matrix elements on the ionic potential. For furthur comparison of these angular distributions as the wave packet moves through the crossing, the lower left panel of Fig. 11 shows the angular distribution at the peak energy of each spectrum.

The energy-integrated angular distributions of photoelectrons for pump–probe delays of 1050, 1125, and 1200 fs and with the probe polarization parallel to the molecular axis of Fig. 12 serve as a final example. As the wave packet moves into and through the crossing, the characteristic $d_z^2$ angular distribution of the photoelectron evolves from one that is more symmetrical with respect to ejection from the Na and I sides of the molecule at 1050 fs to one that strongly favors ejection from the I side.

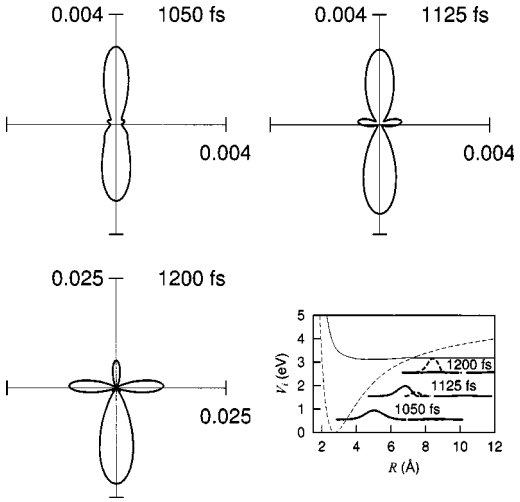


FIG. 12. Polar plots of the energy-integrated angular distributions and snapshots of the wave packet moving through the crossing. Probe polarization parallel to that of the pump.

## IV. CONCLUDING REMARKS

In this paper we have discussed the requisite extension of our theory of energy- and angle-resolved photoelectron spectra for pump–probe ionization of molecules[13] to study wave packet motion on the nonadiabatically coupled ionic ($Na^+I^-$) and covalent (NaI) states of sodium iodide. A principal objective of these studies has been to explore the potential of such pump–probe photoelectron spectra for direct observation of wave packet bifurcation due to a nonadiabatic transition and for probing the intramolecular electron transfer that occurs in the crossing region between the covalent and ionic states. The results of these studies suggest that the energy and angular distributions of such photoelectron spectra do indeed map the motion and bifurcation of the wave packet through the crossing region and should provide a useful window on the intramolecular electron transfer occurring between the covalent and ionic states ($NaI \rightarrow Na^+I^-$) in the nonadiabatic region. Use of robust values of the photoionization amplitudes and their evolution with internuclear distance through the crossing region, however, is essential in such studies. While in this paper we have focused on the behavior of pump–probe photoelectron spectra in the crossing region, these spectra provide useful insight on the wave packet dynamics in other regions of these potential surfaces—e.g., near the right- and left-turning points on the ionic and covalent potentials, respectively. These results will be the subject of a future paper.[27]

## ACKNOWLEDGMENTS

This work was supported by grants from the 21st Century COE Program for Frontiers in Fundamental Chemistry of the Ministry of Education, Culture, Sports, Science, and Technology (Japan), the Mitsubishi Foundation, and the National Science Foundation (U.S.).

[1] M. Seel and W. Domcke, J. Chem. Phys. **95**, 7806 (1991).
[2] Ch. Meier and V. Engel, J. Chem. Phys. **101**, 2673 (1994).
[3] I. Fischer, D. M. Villeneuve, M. J. J. Vrakking, and A. Stolow, J. Chem. Phys. **102**, 5566 (1995).
[4] A. Assion, M. Geisler, J. Helbing, V. Seyfried, and T. Baumert, Phys. Rev. A **54**, R4605 (1996).
[5] C. P. Schick, S. D. Carpenter, and P. M. Weber, J. Phys. Chem. A **103**, 10470 (1999).
[6] C. Jouvet, S. Martrenchard, D. Solgadi, *et al.* J. Phys. Chem. A **101**, 2555 (1997).
[7] V. Blanchet, M. Z. Zgierski, T. Seideman, and A. Stolow, Nature (London) **401**, 52 (1999).
[8] J. A. Davies, J. E. LeClaire, R. E. Continetti, and C. C. Hayden, J. Chem. Phys. **111**, 1 (1999).
[9] L. Wang, H. Kohguchi, and T. Suzuki, Faraday Discuss. **113**, 37 (1999).
[10] D. M. Neumark, Annu. Rev. Phys. Chem. **52**, 255 (2001).
[11] K. Resch, V. Blanchet, A. Stolow, and T. Seideman, J. Phys. Chem. A **105**, 2756 (2001).
[12] V. Blanchet, S. Lochbrunner, M. Schmitt, J. P. Shaffer, J. J. Larsen, M. Z. Zgierski, T. Seideman, and A. Stolow, Faraday Discuss. **115**, 33 (2000).
[13] Y. Arasaki, K. Takatsuka, K. Wang, and V. McKoy, J. Chem. Phys. **112**, 8871 (2000).
[14] T. Seideman, J. Chem. Phys. **113**, 1677 (2000).

[15] K. Takatsuka, Y. Arasaki, K. Wang, and V. McKoy, Faraday Discuss. **115**, 1 (2000).
[16] T. Seideman, Phys. Rev. A **64**, 042504 (2001).
[17] Ch. Meier and V. Engel, Chem. Phys. Lett. **212**, 691 (1993); M. Braun, Ch. Meier, and V. Engel, J. Chem. Phys. **105**, 530 (1996).
[18] Y. Arasaki, K. Takatsuka, K. Wang, and V. McKoy, Chem. Phys. Lett. **302**, 363 (1999).
[19] Y. Arasaki, K. Takatsuka, K. Wang, and V. McKoy, J. Electron Spectrosc. Relat. Phenom. **108**, 89 (2000).
[20] See, for example, M. Gruebele and A. Zewail, J. Chem. Phys. **98**, 883 (1993).
[21] R. R. Lucchese, G. Raseev, and V. McKoy, Phys. Rev. A **25**, 2572 (1982); R. R. Lucchese, K. Takatsuka, and V. McKoy, Phys. Rep. **131**, 147 (1986).
[22] T. S. Rose, M. J. Rosker, and A. H. Zewail, J. Chem. Phys. **88**, 6672 (1988).
[23] For example, P. Cong, G. Roberts, J. L. Herek, A. Mohktari, and A. H. Zewail, J. Phys. Chem. **100**, 7832 (1996).
[24] A. H. Zewail, *Femtochemistry: Ultrafast Dynamics of the Chemical Bond* (World Scientific, Singapore, 1994), Vols. 1 and 2.
[25] E. Charron and A. Suzor-Weiner, J. Chem. Phys. **108**, 3922 (1998).
[26] G. Grégoire, M. Mons, I. Dimicoli, F. Piuzzi, E. Charron, C. Dedonder-Lardeux, C. Jouvet, S. Martrenchard, D. Solgadi, and A. Suzor-Weiner, Eur. Phys. J. D **1**, 187 (1998).
[27] Y. Arasaki, K. Takatsuka, K. Wang, and V. McKoy (unpublished).